Light-reinforced key intermediate for anti-coking to boost highly durable methane dry reforming over single atom Ni active sites on CeO_2

Zhiqiang Rao[ab ‡], Kaiwen Wang[c ‡], Yuehan Cao[b], Yibo Feng[c], Zeai Huang[b]*, Yaolin Chen[b], Shiqian Wei[d], Luyu Liu[b], Zhongmiao Gong[e], Yi Cui[e], Lina Li[f], Xin Tu[g], Ding Ma[h], and Ying Zhou[ab]*

[a] State Key Laboratory of Oil and Gas Reservoir Geology and Exploitation, Southwest Petroleum University, Chengdu 610500, People's Republic of China

[b] School of New Energy and Materials, Southwest Petroleum University, Chengdu 610500, People's Republic of China

[c] Beijing Key Lab of Microstructure and Properties of Advanced Materials, Beijing University of Technology, Beijing 100020, People's Republic of China

[d] China School of Chemistry, Resource and Environment, Leshan Normal University, Leshan 614000, People's Republic of China

[e] Vacuum Interconnected Nanotech Workstation, Suzhou Institute of Nano-Tech and Nano-Bionics, Chinese Academy of Sciences, Suzhou 610500, People's Republic of China

[f] Shanghai Synchrotron Radiation Facility, Shanghai Advanced Research Institute, Chinese Academy of Sciences, Shanghai 201210, People's Republic of China

[g] Department of Electrical Engineering and Electronics University of Liverpool, Liverpool L69 3GJ, United Kingdom

[h] Beijing National Laboratory for Molecular Sciences, College of Chemistry and Molecular Engineering and College of Engineering, Peking University, Beijing 100871, People's Republic of China

*E-mail: zeai.huang@swpu.edu.cn

*E-mail: yzhou@swpu.edu.cn

‡Z.R. and K.W. contributed equally to this paper.

ABSTRACT: Dry reforming of methane (DRM) has been investigated for more than a century, the paramount stumbling block in its industrial application is the inevitable sintering of catalysts and excessive carbon emissions at high temperatures. However, the low-temperature DRM process still suffered the poor reactivity and severe catalyst deactivation from coking. Herein, we proposed a concept that highly durable DRM could be achieved at low temperatures via fabricating the active sites integration with light irradiation. The active sites with Ni-O coordination (Ni_{SA}/CeO_2) and Ni-Ni coordination (Ni_{NP}/CeO_2) on CeO_2, respectively, were successfully constructed to obtain two targeted reaction paths that produced the key intermediate (CH_3O*) for anti-coking during DRM. In particular, the *operando* diffuse reflectance infrared Fourier transform spectroscopy coupling with steady-state isotopic transient kinetic analysis (*operando* DRIFTS-SSITKA) was utilized and successfully tracked the anti-coking paths during DRM process. It was found that the path from CH_3* to CH_3O* over Ni_{SA}/CeO_2 was the key path for anti-coking. Furthermore, the targeted reaction path from CH_3* to CH_3O* was reinforced by light irradiation during the DRM process. Hence, the Ni_{SA}/CeO_2 catalyst exhibits excellent stability with negligible carbon deposition for 230 h under thermo-photo catalytic DRM at a low temperature of 472 ℃, while Ni_{NP}/CeO_2 shows apparent coke deposition behavior after 0.5 h in solely thermal-driven DRM. The findings are vital as they provide critical insights into the simultaneous achievement of low-temperature and anti-coking DRM process through distinguishing and directionally regulating the key intermediate species.

■ INTRODUCTION

Dry reforming of methane (DRM, $CH_4 + CO_2 \rightarrow 2CO + 2H_2$ ΔH_{298K}=247 kJ mol^{-1}) is a promising approach to fixing the top two greenhouse gases with intangible carbon emissions.[1-2, 3-6] However, no commercial process is available, mainly attributed to high energy consumption coupled with the lack of highly

durable catalysts. Many efforts have been made for that over the past decades; *Song et al.* reported that Ni-Mo nanocatalysts on single-crystalline MgO exhibited durability for 850 h, but the input temperature required up to 800 °C.[7] The high energy penalty (1100 °C) is unavoidable, although molten metal alloys were proposed not to be affected by coking.[1] The activation of CH_4 and CO_2 during DRM was achieved under low temperatures, while fast deactivation of catalysts would occur due to the coking deposition resulting from the side reactions involving either CH_4 or CO_2.[8-10] The contradiction between low reaction temperatures and anti-coking is an enormous stumbling block for its application.

Intermediate species are vital for achieving anti-coking DRM because the slight change in the interplay of catalyst-adsorbate can lead to a considerable alteration in the overall catalytic process.[11] The methoxy (CH_3O*) has been commonly proposed to be a crucial intermediate for avoiding coke deposition by the density functional theory (DFT) studies.[12-14] Nevertheless, unraveling the active centers and unlocking the generating pathway of CH_3O* intermediate to achieve durable activity during the DRM process are still to be black boxes. The difficulty arises that both CH_4 and CO_2 reactants are the sources of carbon-containing intermediates, which results in multi-side reactions simultaneously producing CH_3O*, including the oxidation of methyl (CH_3* + O* → CH_3O*) and hydrogenation of carbon dioxide (CO_2* + 5H* → CH_3O* + H_2O*). Therefore, the CH_3O* intermediate during the DRM process cannot be disentangled from the parallel reaction pathways by conventional spectroscopic techniques.[15-16] More seriously, both the dissociation of CH_4 and the activation of CO_2 could involve in carbon depostion,[17] which are much faster than the rate of CH_3O* intermediate formation at low temperature, whereby leading to the heavy carbon deposition. Recent studies revealed that the targeted active intermediate could be enhanced by the external field.[18] For instance, *Lee et al* attributed the enhanced CO_2 hydrogenation activity due to the light irradiation promoting CO_2 intermediate dissociation on the Ru surface.[19] *Scott et al*. revealed that the light-enhanced formate (HCO_2*) intermediate species achieved an eightfold improvement of the Sabatier reaction rates on $NiO_x/La_2O_3@TiO_2$.[20]

Herein, low-temperature DRM with high durability was achieved *via* constructing the targeted active center in combination with the light irradiation. Two reaction paths, the oxidation of CH_3* and the hydrogenation of CO_2, during the DRM process were achieved by designing the Ni-O and Ni-Ni active sites, respectively. More importantly, for the first time we revealed that the active sites with Ni-O coordination was favorable to convert CH_3* into CH_3O* and subsequently produced CO and H_2, thus exhibiting no coking behaviors, while the CH_3O* generating from the hydrogenation of CO_2 results in coking over the active center with Ni-Ni coordination through the *operando* diffuse reflectance infrared Fourier transform spectroscopy coupling with steady-state isotopic transient kinetic analysis (*operando* DRIFTS-SSITKA). Furthermore, the path from CH_3* to CH_3O* over the Ni-O site was reinforced by light irradiation, which accelerated the generation and conversion of CH_3O* during the DRM process. As a result, the catalyst with Ni-O coordination showed stability for 230 h with negligible carbon deposition in thermo-photo catalytic DRM at 472 °C, while the catalyst Ni-Ni coordination exhibited distinct coke deposition behavior after 0.5 h in thermal catalytic DRM.

■ EXPERIMENTAL SECTION

Materials. The nickel nitrate hexahydrate ($Ni(NO_3)_2{\cdot}6H_2O$) and cerium nitrate hexahydrate ($Ce(NO_3)_3{\cdot}6H_2O$) were 99.99% and 99.95%, respectively. The sodium hydroxide (NaOH) was ≥ 98%. The CeO_2 nanorods were obtained with the hydrothermal method.[21] The sodium hydroxide solution (C_{NaOH} = 0.01 mol L^{-1}, 35 mL) was added to cerium nitrate solution (0.868 g of $Ce(NO_3)_3{\cdot}6H_2O$ in 5 mL of deionized H_2O) by drops and stirred for 30 min, then, transferred the white precipitates into a 100 mL Teflonlined stainless-steel autoclave and hydrothermally heated for 24 h at 100 °C. After centrifugation and drying, the obtained samples were calcined at 600 °C for 2 h in an air atmosphere. The Ni was loaded on the surface of CeO_2 using a wet impregnation method. In more detail, 1.0 g of CeO_2 was added into 50.0 mL of an aqueous solution of 0.049 g and 0.148 g of $Ni(NO_3)_2{\cdot}6H_2O$ to obtain Ni_{SA}/CeO_2 and Ni_{NP}/CeO_2 catalyst, respectively. Then, the extra water was evaporated at 80 °C until dryness. After that, the mixture was calcined at 400 °C for 2 h under air.

Catalytic reactions. The thermo-photo and thermal catalytic reactions were measured at atmospheric pressure in a Harrick cell reactor with a flat cover and a quartz window. The intensity range of the UV-vis irradiation (320-800nm, PerfectLight PLS-FX300HU) focused on the reactor was 1.1-2.4 W cm^{-2} with a 1.0 cm diameter of the irradiation spot. All the gases used in this study were 99.99%. Before the catalytic reaction, the catalysts were *in situ* oxidized in the cell with 5 vol% O_2/Ar with a flow rate of 80 mL min^{-1} controlled by a mass flow controller (Bronkhorst) at 450 °C for 30 min. Then, the catalysts were *in situ* reduced with 5 vol% H_2/Ar with a flow rate of 80 mL min^{-1}, controlled by a mass flow controller (Vögtlin), at 450 °C for 30 min. After that, the catalysts were cooled down to room temperature in the H_2/Ar atmosphere. A feed stream of 20 vol% CH_4 and 20 vol% CO_2 balanced with Ar controlled by mass flow controllers (Vögtlin) continuously flowed through the reactor at a flow rate of 10 mL min^{-1}, respectively. The reaction gases and production gases were analyzed by using gas chromatography (Shimadzu GC-8A) equipped with a thermal conductivity detector (TCD) and flame ionization detector (FID), and a mass spectrometer (OmniStar GSD-320, Pfeiffer Vacuum).

***In situ* Raman spectra.** The *in-situ* Raman spectra were performed by a high-resolution Raman spectrometer system (Horiba LabRam HR) equipped with 473 nm laser excitations in a Harrick Raman high-temperature reaction chamber with a 25 mm thick mica window facing the incoming laser. The spectra recording process is consistent with the thermo-photo and thermal catalytic DRM reaction. For the $CH_4/C^{18}O_2$ experiments, the Ni/CeO_2 sample was pretreated with O_2 and H_2, respectively, at 450 °C for 30 min. Then, the gas was switched from $C^{16}O_2/CH_4$/Ar to $C^{18}O_2/CH_4$/Ar after being reacted for 30 min. The Raman spectra were collected after 5, 10, and 15min.

The *operando* DRIFTS coupled SSITKA. The *operando* DRIFTS coupled SSITKA measurements were carried out on a Bruker infrared spectrometer (Tensor II) equipped with a liquid nitrogen-cooled mercury-cadmium-telluride (MCT) detector in a three-window diffuse-reflectance cell (Harrick Praying Mantis) with ZnSe windows. The infrared data were accumulated by recording 100 scans with a resolution of 4 cm^{-1}. The Ni/CeO_2 catalyst (25 mg) was gently pressed onto an inert metal mesh covered with silica (30 mg, 100-200 μm) at the bottom of the sample holder, and the outlet gas was detected by a mass spectrometer (OmniStar GSD-320, Pfeiffer Vacuum). For CO probe

experiments, the Ni/CeO_2 sample was pretreated with O_2 and H_2, respectively, at 450 ℃ for 30 min. The background spectra of CO adsorption experiments were recorded in pure Ar gas (controlled by Vögtlin mass flow controller), purging the pretreated catalysts for 30 min, at 10 ℃. Then, the catalysts were exposed to 10 vol% CO/Ar with a flow of 10 mL min^{-1} (controlled by KOFLOC mass flow controller) at 10 ℃. For the DRIFTS-SSITKA, the background spectra were obtained by purging the pretreated catalysts in pure Ar gas for 30 min. The gas composition and flow rate aligned with the catalytic tests.

The XPS characterization. The NAP-XPS spectra were recorded on a commercial SPECS AP-XPS chamber equipped with a PHOIBOS 150 NAP hemispherical analyzer and monochromatic SPECS μ-FOCUS 600 NAP X-ray source, Al Kα line (hv = 1486.6 eV). The Ni/CeO_2 powder was pressed on a copper plate and then loaded into the AP-XPS chamber. After the thermo-photo DRM reaction in the NAP-XPS chamber, the catalysts were transferred to an XPS chamber (Thermo ESCALAB Xi+) through the Vacuum Interconnected Nanotech Workstation in Suzhou (Nano-X). Then, the quasi *in situ* XPS measurements were performed emission with Al Kα at 1486.6 eV. All the binding energies were corrected with reference to the C 1s at 284.8 eV.

■ RESULTS AND DISCUSSION

The synthesis and structural characterizations of the Ni species on ceria. CeO_2 was chosen as the catalyst support because of its capacity to uptake and release oxygen, benefiting from the rapid and reversible transformation between Ce^{3+} and Ce^{4+}.[22-24] Nickel is commonly considered to be the active component owing to the impressive ability to break the C-H bond of CH_4.[25-26] The Gibbs free energy change (ΔG) of the catalyst with Ni-O coordination from DFT calculations indicates that the first C-H bond cleavage on CH_4 at low temperature (-1.94 eV) is thermodynamic favorable (Figure S1a and Table S1). More importantly, the formed CH_3* is favorable to react with the oxygen to form CH_3O* instead of cleaving on the Ni-O site (Figure S1b, Table S2 and S3). In contrast, on the Ni-Ni site, the CH_3* species is more inclined to form CH_2* and H* (Figure S1c, Table S2 and S3). Furthermore, combined with the density of states (DOS), the formation of Ni-O coordination on the catalyst surface significantly weakens the Ce-O bonds, which accelerates lattice oxygen to be involved in the formation process of CH_3O* (Figure S2). These results demonstrate that the targeted design of Ni-O active site can produce CH_3O* species through the path of CH_3* oxidation, while this is unfavorable over the Ni-Ni active site. Therefore, we constructed the active sites with Ni-O coordination by atomically dispersing Ni atoms (Ni_{SA}/CeO_2) on the CeO_2 matrix. Meanwhile, the reference catalyst with Ni-Ni coordination was prepared by fixing Ni nanoparticles

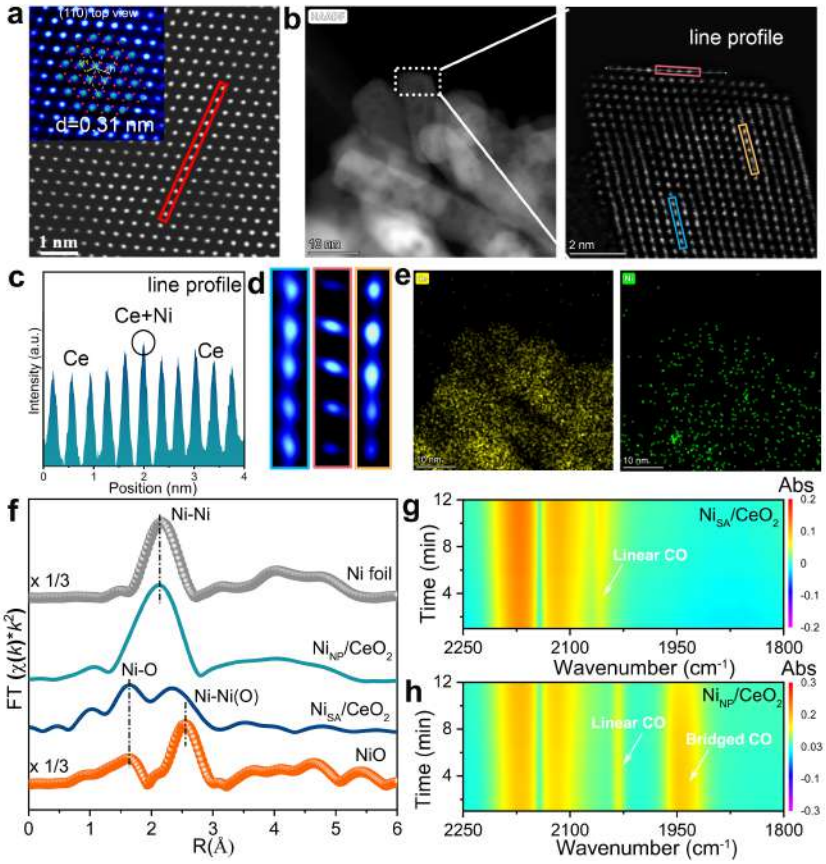

Figure 1. Microstructures and coordination environment of the CeO_2, Ni_{SA}/CeO_2, and Ni_{NP}/CeO_2. (**a**) The high-resolution high-angle annular dark-field scanning transmission electron microscopy (HR-HAADF-STEM) image of CeO_2, (**b**) the HR-HAADF-STEM images, (**c**) the corresponding intensity profiles of the scans, (**d**) the amplified resolution image, (**e**) the energy dispersive spectrometry (EDS) elemental mapping images of Ni_{SA}/CeO_2 catalyst after H_2 pretreated at 450 ℃. (**f**) The corresponding k^2-weighted Fourier transform extended X-ray absorption fine structure (EXAFS) spectra in R space of Ni_{SA}/CeO_2 and Ni_{NP}/CeO_2 after H_2 pretreated at 450 ℃. The *in situ* DRIFTS of CO chemisorption at 10 ℃ on (**g**) Ni_{SA}/CeO_2, and (**h**) Ni_{NP}/CeO_2 after H_2 pretreated at 450 ℃.

(Ni_{NP}/CeO_2) on the CeO_2 support. The details of catalyst preparation were presented in the experimental sections. The surface areas S_{BET} of Ni_{SA}/CeO_2 and Ni_{NP}/CeO_2 catalysts are 74 m^2/g and 71 m^2/g, respectively (Figure S3). The loading of Ni in Ni_{SA}/CeO_2 and Ni_{NP}/CeO_2 catalysts is 0.76 wt% and 2.61 wt%, respectively by inductively coupled plasma optical emission spectroscopy (ICP-OES). The diffraction peaks in the X-ray diffraction (XRD) patterns of Ni_{SA}/CeO_2 and Ni_{NP}/CeO_2 catalysts are characteristic of the typical fluorite structure of CeO_2; no signals attributed to NiO and Ni metal were observed (Figure S4). In addition, no NiO and Ni nanoparticles reflections could be found in the ultraviolet-visible diffuse (UV-vis) absorption spectrum of Ni_{SA}/CeO_2 (Figure S5), which indicates the high dispersion of Ni on CeO_2.

The fabricated CeO_2 showed nanorod morphology (Figure S6). The HR-HAADF-STEM images (Figure 1a) show the lattice fringes of CeO_2, with an interplanar spacing of 0.31 nm, corresponding to the (111) plane of CeO_2.[27-28] For Ni_{SA}/CeO_2, the Ni atom cannot be observed from the HR-HAADF-STEM images due to its much lighter element than Ce (Figure 1b). Meanwhile, the bright dots with higher contrast than the surrounding CeO_2 lattice observed in Figure 1c and d may be attributed to the overlapping Ni and Ce atoms. Furthermore, the Ni species maintained highly dispersed on the CeO_2 nanorods from the mapping result (Figure 1e). In contrast, the pronounced agglomeration of Ni with particle size ~10 nm can be observed in the Ni_{NP}/CeO_2 catalyst (Figure S7). The Ni-O coordination of Ni_{SA}/CeO_2 catalyst was confirmed in Ni K-edge XANES spectra (Figure S8). In contrast, it exhibits a marked decrease in Ni_{NP}/CeO_2. The EXAFS fitting curves and structures (optimized by DFT) of Ni_{SA}/CeO_2 and Ni_{NP}/CeO_2 (Figure 1f, S9, and Table S4) implied two signals at approximately 1.87 Å (C.N. = 2.0) and 2.40 Å (C.N. = 2.0) assigned to Ni-O and Ni-Ce scattering, respectively, are unambiguously observed for the Ni_{SA}/CeO_2. No contribution of Ni-Ni scattering could be found, which confirms that the Ni species is atomically dispersed on the surface of CeO_2 nanorods with the Ni-O coordination in Ni_{SA}/CeO_2. In contrast, a Ni-Ni contribution at 2.16 Å (C.N. = 3.0) is observed in Ni_{NP}/CeO_2, indicating the presence of Ni-Ni coordination.[12] Furthermore, the wavelet transformation (WT) exhibited significant Ni-Ni contribution in Ni_{NP}/CeO_2, while only a Ni-O contribution was found for Ni_{SA}/CeO_2 (Figure S10).[29-30]

The *in situ* DRIFTS of CO chemisorption revealed that the Ni_{SA}/CeO_2 catalyst only exhibited a linearly adsorbed CO peak (2064 cm^{-1}) on Ni species (Figure 1g, and S11),[31-32] while the spectrum of Ni_{NP}/CeO_2 catalyst showed a remarkably bridged-CO peak at 1945 cm^{-1} due to the interplay of CO with the Ni nanoparticles (Figure 1h).[32-33] The above results corroborated that the Ni atomically dispersed on CeO_2 nanorods over Ni_{SA}/CeO_2 catalyst with Ni-O coordination, while the Ni species exist on the surface of CeO_2 nanorods as nanoparticles over Ni_{NP}/CeO_2 with Ni-Ni coordination. Moreover, the Ce L-edge XANES indicates a stronger interplay of the orbitals in Ni_{SA}/CeO_2 than that in Ni_{NP}/CeO_2 between CeO_2 matrix and Ni species (Figure S12 and Table S5). Similar results can also be found in the electron paramagnetic resonance (EPR) spectra (Figure S13a) and the H_2 temperature-programmed reduction (H_2-TPR, Figure S13b). Therefore, the strong electronic metal-support interaction (EMSI) between atomically dispersed Ni and CeO_2 over Ni_{SA}/CeO_2 with Ni-O coordination could occur due to the tremendous electronic perturbation on the interface, which contributes to anchoring the atomically dispersed Ni on the surface of CeO_2 and also for the more robust oxygen migration capacity than Ni_{NP}/CeO_2 with Ni-Ni coordination.

The catalytic performances and anti-coking ability of DRM reactions.

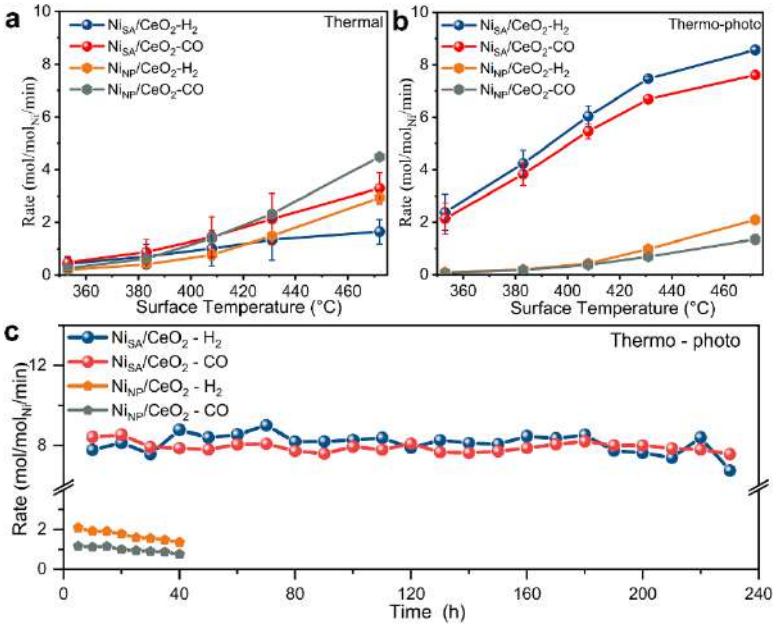

Figure 2. The performances and anti-coking ability of Ni_{SA}/CeO_2 and Ni_{NP}/CeO_2 catalysts in DRM reaction. (**a**) H_2 and CO yields under thermal catalysis. (**b**) H_2 and CO yields under thermo-photo catalysis. (**c**) The long-term stability of the thermo-photo catalytic DRM reaction over Ni_{SA}/CeO_2 and Ni_{NP}/CeO_2 catalysts at 472 °C. Reaction conditions: $CH_4/CO_2/Ar$=1/1/3, a total flow rate of 20 mL min^{-1}, 25 mg catalyst, 300 W Xe lamp.

The DRM catalytic reaction rate shows an ignorable increment between Ni-O and Ni-Ni coordination under thermal catalytic condition (Figure 2a, S14a, and b). Interestingly, under thermo-photo conditions at the same surface temperature as thermal catalytic condition, calibrating by the thin contact thermometer with K-thermocouple (Figure S15), the Ni_{SA}/CeO_2 catalyst provided a significantly higher catalytic reaction rate than that of the Ni_{NP}/CeO_2 catalyst (Figure 2b, S14c, and d). Specifically, under thermo-photo catalytic conditions at 472 °C, the yields of H_2 and CO for Ni_{SA}/CeO_2 catalyst achieve 8.56 mol mol_{Ni}^{-1} min^{-1}, and 7.68 mol mol_{Ni}^{-1} min^{-1}, respectively, which are approximately four times higher than those for Ni_{NP}/CeO_2 catalyst (1.97 mol mol_{Ni}^{-1} min^{-1}, and 1.22 mol mol_{Ni}^{-1} min^{-1}, respectively). More importantly, with light irradiation, the conversion of CH_4 and CO_2 increased from 8.8% and 9.4% to 16.5% and 16.2%, respectively, which breaks the limitation of thermodynamic equilibrium at the same temperature (Figure S16). This was evidenced via near-ambient-pressure (NAP) X-ray photoelectron spectroscopy (XPS), whereby the CH_x groups and carbonate species on Ni/NiO were detected in the spectra of both Ni_{SA}/CeO_2 and Ni_{NP}/CeO_2,[34] and the light irradiation accelerated the conversion of CH_4 and CO_2 (Figure S17). Meanwhile, the light-to-chemical energy reached 1.6% at 2.4 W cm^{-1}, which was higher than that reported under a similar light intensity.[35] The conversion rate of CH_4 and CO_2 were 14.1 μmol min^{-1} and 14.9 μmol min^{-1}, respectively; the generation amount of CO was 27.7 μmol min^{-1}, indicating a carbon balance of 0.96 that was close to the theoretical number of 1.0. The ratio of H_2/CO decreases with the rising of temperatures in thermal catalytic DRM reaction for both Ni_{SA}/CeO_2 and Ni_{NP}/CeO_2 catalysts due to the occurrence of reverse water gas shift (RWGS) reaction. On the contrary, the H_2/CO ratio was always maintained at *ca.* 1.0 for Ni_{SA}/CeO_2 catalyst, and it also tends to increase with the temperatures rising for Ni_{NP}/CeO_2 catalyst in thermo-photo condition (Figure S18), which is consistent with the reported phenomenon.[36] In particular, the performance of Ni_{SA}/CeO_2 is impressively stable under the thermo-photo catalytic DRM reaction at 472 °C even after 230 h (Figure 2c), which showed excellent stability among the thermal and thermo-photo catalytic DRM at a temperature less than 600 °C (Table S6 and S7). In comparison, a rapid decrease was found for Ni_{NP}/CeO_2 when the reaction was performed under the thermo-photo condition. In addition, both the Ni_{SA}/CeO_2 and Ni_{NP}/CeO_2 catalysts showed apparent deactivation phenomena in the thermal-driven DRM process (Figure S19).

The deactivation of catalysts in DRM can be attributed to two factors, including the coke depositing on the active sites and the sintering of active metals. The EXAFS spectra of Ni K-edge over Ni_{SA}/CeO_2 during thermo-photo catalytic DRM reaction after 230 h still maintained the Ni-O coordination (Figure 3a and S20). Also, no Ni^0 signals appeared from the results of XPS of Ni $2p_{3/2}$ (Figure 3b and S21).[13, 34] These results demonstrate that the Ni species over Ni_{SA}/CeO_2 catalyst still maintained the Ni-O coordination without any agglomeration during thermo-photo catalytic DRM reaction. Besides, the Ni_{SA}/CeO_2 catalyst after reaction exhibited lower O_2 consumption and CO_2 production than Ni_{NP}/CeO_2 (Figure S22), indicating that the deactivation of catalysts may be caused by coke deposition. Importantly, there was a negligible carbon deposition on the Ni_{SA}/CeO_2 catalyst even after the 230-h reaction under thermo-photo conditions (Figure 3c). Meanwhile, no carbon nanotubes were detected in TEM (Figure 3d). However, after thermo-photo catalytic DRM reaction over Ni_{NP}/CeO_2, apparent coke deposition and carbon nanotubes were observed (Figure 3c and e).[15, 37] This also reflected on the catalytic activity that Ni_{NP}/CeO_2 showed much lower active rate during thermo-photo DRM process. In

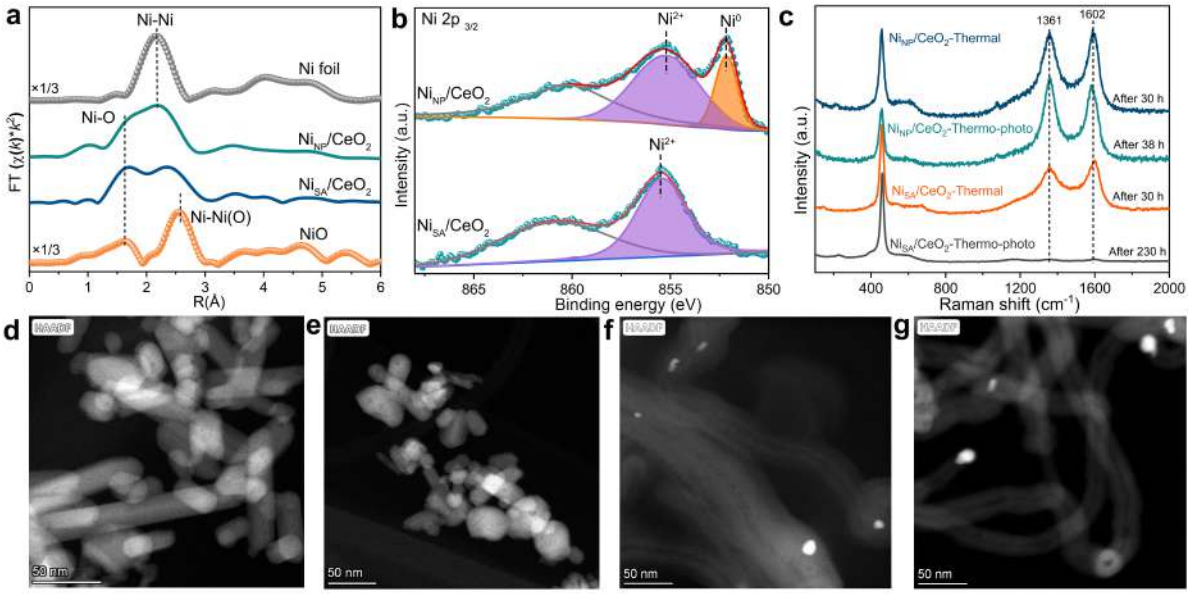

Figure 3. The microstructures and coordination environment of Ni_{SA}/CeO_2 and Ni_{NP}/CeO_2 after the DRM reaction process. (**a**) The corresponding k^2-weighted EXAFS spectra of Ni K-edge Ni_{SA}/CeO_2, and Ni_{NP}/CeO_2 after thermo-photo catalytic DRM reaction. (**b**) The quasi *in situ* XPS of the Ni_{SA}/CeO_2 and Ni_{NP}/CeO_2 after thermo-photo catalytic DRM reaction. (**c**) The Raman spectra (λ_{ex}=473 nm) of Ni_{SA}/CeO_2 and Ni_{NP}/CeO_2 catalyst after thermal and thermo-photo catalytic DRM reaction, respectively. The TEM images of (**d**) Ni_{SA}/CeO_2 and (**e**) Ni_{NP}/CeO_2 after the long-term stability test under thermo-photo condition, and the TEM images of (**f**) Ni_{SA}/CeO_2 and (**g**) Ni_{NP}/CeO_2 after the long-term stability test under thermal condition.

the absence of light irradiation, an evident coking phenomenon and carbon nanotubes can be observed both in Ni_{SA}/CeO_2 and Ni_{NP}/CeO_2 (Figure 3f and g). The dynamic carbon deposition analysis from *in-situ* Raman indicated that the cracking rate of CH_4 over Ni_{NP}/CeO_2 was faster than that over Ni_{SA}/CeO_2 (Figure S23a and b). Furthermore, for the Ni_{SA}/CeO_2 catalyst, no characteristic peak associated with coke deposition was observed from 193 ℃ to 472 ℃ under thermo-photo catalysis from *in-situ* Raman (Figure S23c). Considering that the coking degree is highly correlated to the CH_4 conversion. We compared the stability of thermo-photo catalytic DRM under the similar CH_4 conversion (19%) over Ni_{SA}/CeO_2 (Figure S24a) and Ni_{NP}/CeO_2 (Figure S24b), respectively. Interestingly, the Ni_{NP}/CeO_2 catalyst showed an obvious deactivation phenomenon, and serious carbon deposition was observed in catalyst after the reaction. The thermogravimetric/differential thermal analysis (TG/DTA) thermograms over Ni_{SA}/CeO_2 and Ni_{NP}/CeO_2, respectively, after long-term stability of the thermo-photo catalytic DRM were obtained to be more quantitative to discuss the amount of coked carbon (Figure S24c). The Ni_{SA}/CeO_2 sample exhibited negligible carbon deposition, while evident coking can be observed in Ni_{NP}/CeO_2. This is consistent with the phenomenon observed in TEM and Raman spectroscopy.

From the above analysis, in the absence of light irradiation, the catalyst with Ni-O coordination occurs apparent deactivation after 8 h due to coke deposition, while the inactivation starts after only 1 h for the catalyst with Ni-Ni coordination. With light irradiation, the coking still occurs on the surface of the catalyst with Ni-Ni coordination, while excellent stability ($>$ 230 h) can be achieved for the catalyst with Ni-O coordination. Therefore, the synergistic effect of both Ni-O coordination and light irradiation is vital to endow the DRM reaction with excellent anti-coking ability.

The effect of Ni-O and Ni-Ni active sites on the anti-coking reaction paths. The *in situ* Raman under thermo-photo conditions in CO and CH_4 gas atmospheres, respectively, over Ni_{SA}/CeO_2 (Figure S25) demonstrated that the coking on the catalyst mainly came from the excessive cracking of CH_4 during the DRM process, consistent with previous work.[35] Especially, the quick dehydrogenation process ($CH_3 \rightarrow CH_2 \rightarrow CH \rightarrow C$) would occur once the initial C-H cleavage of CH_4 ($CH_4 \rightarrow CH_3+H$)[38]. The CH_3O* (path 1, CH_3*+O*→CH_3O*) has been regarded as the critical intermediate to avoid this excessive dehydrogenation process during the DRM process.[12-13] According to the DFT calculation results (Figure S1, Table S2 and S3), the reaction path from CH_3* to CH_3O* is favorable on the active site with Ni-O coordination owing to the superior mobility of CeO_2 surface lattice oxygen atoms (path 1). Meanwhile, the CH_3O* could also be formed through hydrogenating CO_2 (path 2, CO_2*+4H*→CH_3O +OH*) during the DRM process.

However, the contribution of two paths for the anti-coking has never been unlocked during the DRM reaction process. More seriously, the conventional DRIFTS cannot distinguish the CH_3O* reaction pathways due to the CH_3O* is simultaneously

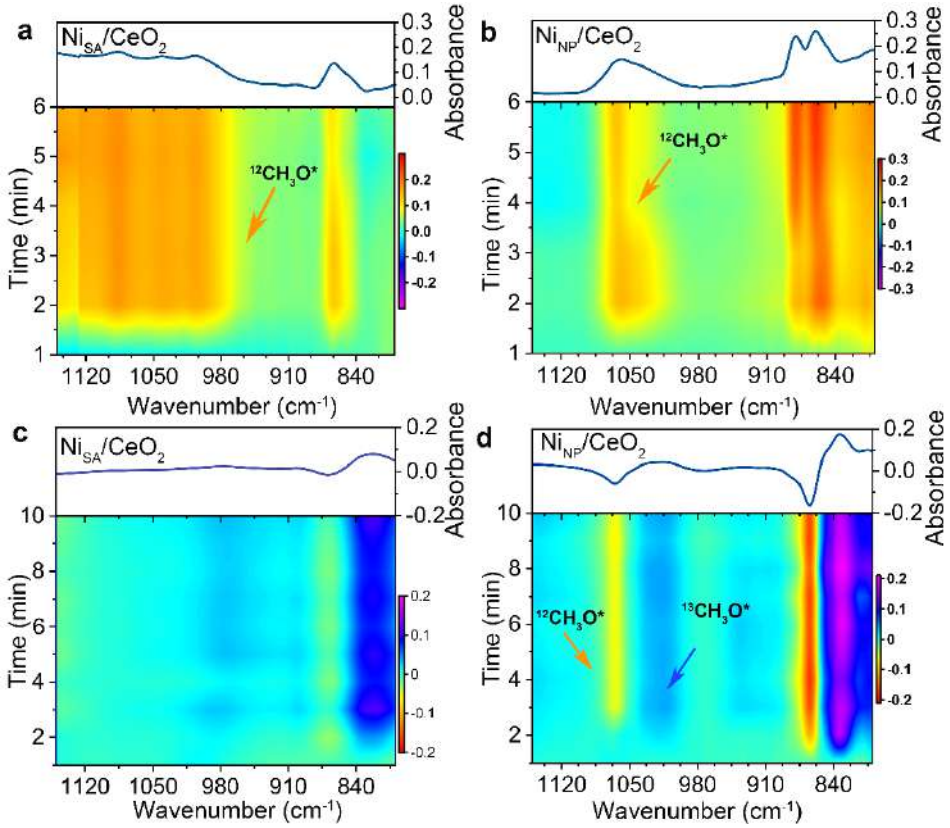

Figure 4. The *operando* DRIFTS-SSITKA of thermo-photo catalytic DRM reaction. The *operando* DRIFTS of (**a**) Ni_{SA}/CeO_2, and (**b**) Ni_{NP}/CeO_2. The *operando* DRIFTS-SSITKA of (**c**) Ni_{SA}/CeO_2, and (**d**) Ni_{NP}/CeO_2 during thermo-photo catalytic DRM reaction at 472 ℃ (light intensity: 2.4 W cm^{-2}). The catalyst was pretreated under an H_2/Ar environment followed by introducing a $^{12}CH_4/^{12}CO_2$/Ar and $^{12}CH_4/^{13}CO_2$/Ar gas mixture (flow rate =20 mL min^{-1}, ratio =1:1:3).

produced from either path 1 or path 2. This further leads to the inability to uncover the reaction pathways of intermediates for anti-coking. To track the surface adsorbates (CH_3O*) and identify the generation path of CH_3O* for anti-coking during the DRM reaction, we devised a highly innovative and unique *operando* DRIFTS coupled SSITKA system. The specific working principle is depicted in Figure S26; By this method, we can successfully decouple the parallel intermediate of CH_3O* pathways that could come from path 1 or path 2.[20, 39-40] Based on this, we can further disclose the contribution of key intermediate (CH_3O*) generation paths for anti-coking.

The DRIFTS and mass spectrometry (MS) data during both the thermal and thermo-photo catalytic DRM were collected over Ni_{SA}/CeO_2 and Ni_{NP}/CeO_2 (Figure S27 and S28). For both the thermal and thermo-photo catalytic DRM process, the MS data demonstrate that the intensities of CH_4 and CO_2 reactants weakly decreased, and the number of products CO and H_2 increased over both Ni_{SA}/CeO_2 and Ni_{NP}/CeO_2 as the temperature increased (Figure S27 a, c, and S28 a, c). The same tendency can also be observed in DRIFTS (Figure S27 b, d and S28 b, d). The noticeable increasing tendency of methoxy species (CH_3O*) was observed over Ni_{SA}/CeO_2 and Ni_{NP}/CeO_2 with the temperature increasing during the thermal and thermo-photo catalytic DRM process in Figure 4 a, b and S29 a, b (marked in the yellow area, from 1010 cm^{-1} to 1084 cm^{-1}).[41-43] The gas was switched from $^{12}CO_2/^{12}CH_4$/Ar to $^{13}CO_2/^{12}CH_4$/Ar after the highest conversion rate was reached and stabilized. The groups related to CO_2 can give rise to pronounced characteristic isotope effect peaks during the reaction re-equilibrating process (marked in the blue area). Interestingly, no isotope effect can be found assigning for the CH_3O* over Ni_{SA}/CeO_2 after switching the gas from $^{12}CO_2$ to $^{13}CO_2$ in the DRIFTS-SSITKA of Ni_{SA}/CeO_2 (Figure S29c). On the contrary, the region attributed to CH_3O* showed an isotope effect for the Ni_{NP}/CeO_2 catalyst in Figure S29d (the blue area located at 1020 cm^{-1}). More critically, with light irradiation, the DRIFTS-SSITKA of Ni_{SA}/CeO_2 exhibit no characteristic isotope effect peaks involving CH_3O* species (Figure 4c), while remarkable isotope signals were detected in Ni_{NP}/CeO_2 in Figure 4d (the blue area). These results reveal that the CH_3O* originated from CH_4 on Ni_{SA}/CeO_2 *via* path 1, while it was produced from the CO_2 over Ni_{NP}/CeO_2 *via* path 2 for both the thermal and thermo-photo catalytic DRM. Also, the DOS of CH_3O* adsorbing on Ni_{SA}/CeO_2 and Ni_{NP}/CeO_2 (Figure S30) indicates that the *d* band center of

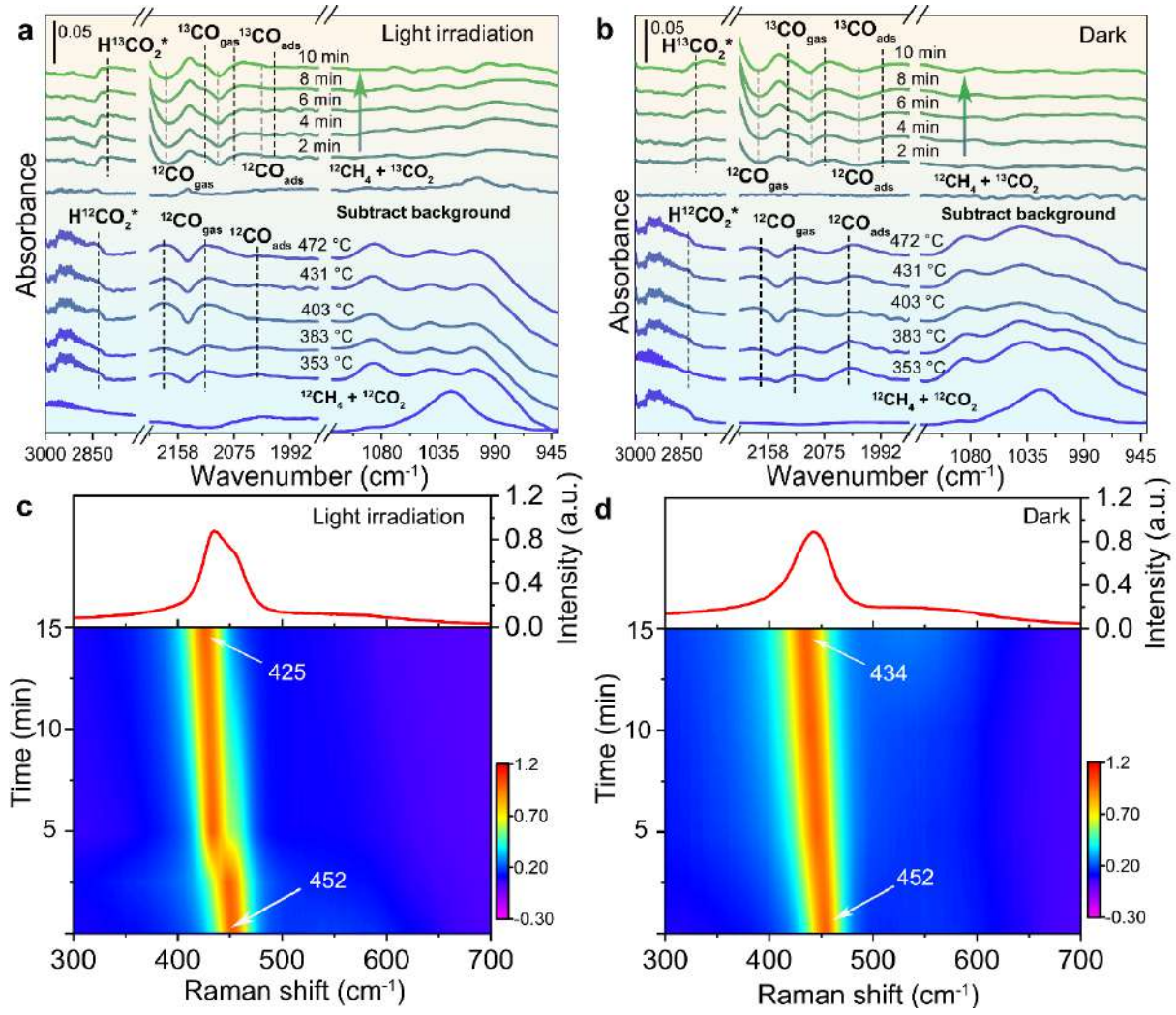

Figure 5. The *operando* DRIFT-SSITKA and *in situ* Raman spectra of DRM reaction over Ni_{SA}/CeO_2. The DRIFTS of DRM process under different temperature (**a**) with light irradiation and (**b**) dark. The *in situ* Raman spectra of DRM process at 472 °C (light intensity: 2.4 W cm^{-2}; flow rate =10 ml min^{-1}, $CH_4/C^{18}O_2$/Ar =1:1:3) (**c**) with light irradiation and (**d**) dark.

Ni_{SA}/CeO_2 (-2.16 eV) exhibits a clear downshift compared with Ni_{NP}/CeO_2 (-1.65 eV). This finding indicates the electrons are more readily transferred to the bonding orbitals of adsorbates (CH_3O*) on Ni_{SA}/CeO_2 than Ni_{NP}/CeO_2, which would accelerate the formation of CH_3O* on Ni_{SA}/CeO_2. Therefore, for Ni_{NP}/CeO_2, the transformation from CH_3* to C* will occur once the first C-H bond of CH_4 is cleaved, eventually producing coking, while the CH_3* will react with coordinated O to produce CH_3O* for Ni_{SA}/CeO_2. All in all, the role of Ni-O coordination structure is responsible for the formation of CH_3O* through oxidizing the CH_3* from CH_4 dehydrogenation with or without light irradiation. Nonetheless, in the absence of light irradiation, the Ni_{SA}/CeO_2 catalyst still suffered from deactivation, which demonstrates that light irradiation also plays a vital role in eliminating coke deposition.

The role of light irradiation for anti-coking over Ni_{SA}/CeO_2. Based on the built *operando* DRIFTS-SSITKA, the contribution of light irradiation during the DRM process over Ni_{SA}/CeO_2 could be revealed. The gaseous CO_2 (2360 cm^{-1}),[44] CH_4 (3013 cm^{-1} and 1301 cm^{-1}),[45] and the adsorbed carbonate/bicarbonate (CO_3*/HCO_3*, 1580 cm^{-1})[46] species gradually decrease as the temperatures increase in both thermal (Figure S27b) and thermo-photo (Figure S28b) catalytic DRM. In particular, with light irradiation, the formate (HCO_2*) species shows a noticeably increasing trend (Figure 5a). The linearly adsorbed CO was gradually reduced due to its desorbing from the surface, meanwhile, the bands of gaseous CO enhanced progressively.[47] However, in the dark, a fragile change was detected (Figure 5b). Moreover, in the case of more abundant gaseous CO for the thermo-photo process, the intensities of linearly adsorbed CO were gradually decreased, while remarkable linearly adsorbed CO was observed with the temperature increased for the DRM without light irradiation (Figure 5 a and b). This phenomenon elucidated that the light irradiation empowers the Ni_{SA}/CeO_2 catalyst with more excellent catalytic activity than that under thermal catalytic DRM by promoting the conversion of carbonates to CO, and the subsequent desorption of CO. More importantly, after switching from $^{12}CO_2/^{12}CH_4/Ar$ to $^{13}CO_2/^{12}CH_4/Ar$, more particularly characteristic isotope effect of gaseous and linearly adsorbed CO could be observed for the DRM process in the dark compared to the process under light irradiation (Figure S31). This indicates that more CO derives from the contribution of path 1 (the process of CH_3O* intermediate) under light irradiation. This further substantiates that light irradiation accelerates the conversion process from CH_3O* to CO. The $C^{18}O_2$ isotope labeling *in-situ* Raman experiments over Ni_{SA}/CeO_2 was performed to further reveal the light contribution to the formation of CH_3O*. The movement of Ce-O signal over time exhibits a more prominent movement under light irradiation (27 cm^{-1}) than that under dark conditions (18 cm^{-1}) during the DRM process (Figure 5 c and d). This demonstrates that the light accelerates coordinated oxygen involving the formation of CH_3O*. Furthermore, the tope labeling experiment ($C^{18}O_2/CH_4$) under thermo-photo condition over Ni_{SA}/CeO_2 was performed at 472 ℃ to make clear how the oxygen of ceria participate in the reaction (Figure S32a). By contrast, the thermal catalytic DRM experiments without light at a higher reaction temperature (500 ℃, 600 ℃, and 700 ℃) were also performed (Figure S32b). With light irradiation, the amount of $C^{16}O$, deriving from the ceria, exhibited an increasing trend, which is much higher than that of in thermal catalytic DRM even at 600 ℃. This demonstrates that the oxygen of ceria participates in the formation process of CO, and light irradiation can accelerate this process. Besides, the formation of CO under light irradiation at 472 °C could be close to that under 600 °C without light irradiation, indicating a significant of light effect on the activity.

Therefore, the path from CH_3* to CH_3O* was essentially determined by the designed Ni single-atom with Ni-O coordination at Ni-CeO_2 interface. Over the Ni_{SA}/CeO_2, the path from CH_3* to CH_3O* was essentially determined by the designed Ni-O sites at the Ni-CeO_2 interface. Meanwhile, light irradiation can promote the generation and conversion of CH_3O* intermediate over Ni_{SA}/CeO_2. The speculated mechanism of thermo-photo catalytic DRM shown in Figure S33, the photo-excited energetic electron generated from the CeO_2 conduction band migrates to the surface and accumulates on the Ni active sites, thereby accelerating the conversion rates by depositing energy to intermediates and further elongating the C=O and C-H bonds. Meanwhile, the photogenerated holes in the valence band of CeO_2 would generate O^{2-} by reacting with coordinated O of the Ni-O site, then reacting with CH_3* to produce CH_3O*. Also, under light irradiation, the photothermal heating from the decay of photogenerated carriers would exacerbate the vibration of the Ni-O bond and elongate the Ni-O bond, which results in the coordinated O would be more likely to migrate out and participate in the formation of CH_3O*. However, the CH_3O* generates from the hydrogenation of CO_2 over Ni_{NP}/CeO_2. This demonstrates produced CH_3* from CH_4 dehydrogenation continues to dehydrogenate rather than participate in the oxidation process, eventually resulting in coking.

Over the past century, DRM is normally performed under high temperatures to achieve a highly durable activity, which heavily hindered the industrial level application. Compared with the previous DRM studies,[48-49] a novel concept that highly durable DRM can be achieved under low temperatures by rationally designing and reinforcing the targeted reaction paths is proposed. The designed catalyst with Ni-O coordination modulated the path of CH_3* to CH_3O* with the assistance of light irradiation, which accelerated the continuous transformation of coordinated oxygen with CH_3*. Furthermore, with the advanced and self-developed *operando* SSITKA-DRIFTS, the key points to achieving stably low-temperature DRM were revealed. Eventually, the huge challenge of low-temperature DRM, the complete dissociation of CH_4 to coke for the covering active sites, was overcome. Besides, the Ni_{SA}/CeO_2 exhibited the DRM performance under concentrated solar energy without external heating input (Figure S34). Therefore, the solar energy could be transferred and stored via this low-temperature DRM process. The built *operando* SSITKA-DRIFTS technology is universal to trace and identify anti-coking intermediates for DRM reaction. The finding on promoting the formation and conversion of anti-coking intermediate opens a door to boost highly stable low-temperature CH_4 utilization. We foresee that this atypically high durability may pave the way toward the creation of feasible approaches and optimized catalysts for the upgradation of CH_4 and CO_2 to value-added compounds.

■ CONCLUSION

In summary, we have demonstrated an effective and promising strategy for the rational design of catalysts in combination with light irradiation to achieve highly stable DRM under low temperatures. A method was developed for the first time to successfully track the origin of the anti-coking intermediate, CH_3O*, during the DRM reaction process by coupling the *operando* DRIFTS and SSITKA. More specially, by constructing and

reinforcing the active sites to produce the critical anti-coking intermediate of CH_3O*, impressive stability of coke resistance catalyst was achieved during DRM reaction at a relatively moderate temperature (472 ℃). Specifically, the generation of anti-coking CH_3O* is attributed to the Ni-O active center, and the light irradiation can accelerate the migration of lattice oxygen to produce CH_3O* and convert it into CO and H_2. As a result, the Ni_{SA}/CeO_2 catalyst exhibits excellent stability for 230 h with negligible carbon deposition, while the Ni_{NP}/CeO_2 catalyst shows distinct coke deposition behavior after 0.5 h. Meanwhile, the yield of H_2 and CO for the Ni_{SA}/CeO_2 catalyst was around four times higher than that for the Ni_{NP}/CeO_2 catalyst under the thermo-photo catalytic DRM process. The mechanistic understanding of modulating the methane activation pathways during DRM reaction can allow us to track the critical carbon-containing intermediates, which involves a multi-parallel reaction in the conversion processes of the C_1 molecule, and pave the way for aiming at the directed transformation of the C-H bond in methane under relatively mild conditions.

■ ASSOCIATED CONTENT

Supporting Information.

Further experimental details, catalyst performance data, and characterization data.

■ AUTHOR INFORMATION

Corresponding Authors

Zeai Huang - *State Key Laboratory of Oil and Gas Reservoir Geology and Exploitation; School of New Energy and Materials, Southwest Petroleum University, Chengdu 610500, China;*
E-mail: zeai.huang@swpu.edu.cn

Ying Zhou - *State Key Laboratory of Oil and Gas Reservoir Geology and Exploitation; School of New Energy and Materials, Southwest Petroleum University, Chengdu 610500, China;*
E-mail: yzhou@swpu.edu.cn

Authors

Zhiqiang Rao - *State Key Laboratory of Oil and Gas Reservoir Geology and Exploitation; School of New Energy and Materials, Southwest Petroleum University, Chengdu 610500, People's Republic of China*

Kaiwen Wang - *Beijing Key Lab of Microstructure and Properties of Advanced Materials, Beijing University of Technology, Beijing 100020, People's Republic of China*

Yuehan Cao - *School of New Energy and Materials, Southwest Petroleum University, Chengdu 610500, People's Republic of China*

Yibo Feng - *Beijing Key Lab of Microstructure and Properties of Advanced Materials, Beijing University of Technology, Beijing 100020, People's Republic of China*

Yaolin Chen - *School of New Energy and Materials, Southwest Petroleum University, Chengdu 610500, People's Republic of China*

Shiqian Wei - *School of New Energy Materials and Chemistry, Leshan Normal University, Leshan 614000, People's Republic of China*

Luyu Liu - *School of New Energy and Materials, Southwest Petroleum University, Chengdu 610500, People's Republic of China*

Zhongmiao Gong - *Vacuum Interconnected Nanotech Workstation, Suzhou Institute of Nano-Tech and Nano-Bionics, Chinese Academy of Sciences, Suzhou 610500, People's Republic of China*

Yi Cui - *Vacuum Interconnected Nanotech Workstation, Suzhou Institute of Nano-Tech and Nano-Bionics, Chinese Academy of Sciences, Suzhou 610500, People's Republic of China*

Lina Li - *Shanghai Synchrotron Radiation Facility, Shanghai Advanced Research Institute, Chinese Academy of Sciences, Shanghai 201210, People's Republic of China*

Xin Tu - *Department of Electrical Engineering and Electronics, University of Liverpool, Liverpool L69 3GJ, United Kingdom*

Ding Ma - *Beijing National Laboratory for Molecular Sciences, College of Chemistry and Molecular Engineering and College of Engineering, Peking University, Beijing 100871, People's Republic of China*

Author Contributions

‡These authors contributed equally

Notes

The authors declare no competing financial interest.

■ ACKNOWLEDGMENT

This research was financially supported by the National Science Fund for Distinguished Young Scholars (52325401), the National key R&D project of China (Grant No. 2020YFA0710000, 2017YFA0403402), National Natural Science Foundation of China (22209136, U1932119), Science and Technology Project of Southwest Petroleum University (2021JBGS10). We thank the Vacuum Interconnected Nanotech Workstation of Suzhou Institute of Nanotech and Nano-bionics, Chinese Academy of Sciences. We thank the help of Dr. Wenchao Wan for the analyzing of XAFS. We thank the staff at the BL11B beamline of the Shanghai Synchrotron Radiation Facilities for assistance with the XAFS.

■ REFERENCES

(1) Palmer, C.; Upham, D. C.; Smart, S.; Gordon, M. J.; Metiu, H.; McFarland, E. W. Dry reforming of methane catalysed by molten metal alloys. *Nat. Catal.* **2020,** 3, 83-89.

(2) Shoji, S.; Peng, X. B.; Yamaguchi, A.; Watanabe, R.; Fukuhara, C.; Cho, Y.; Yamamoto, T.; Matsumura, S.; Yu, M. W.; Ishii, S.; Fujita, T.; Abe, H.; Miyauchi, M. Photocatalytic uphill conversion of natural gas beyond the limitation of thermal reaction systems. *Nat. Catal.* **2020,** 3, 148-153.

(3) Li, J.; He, Y.; Tan, L.; Zhang, P.; Peng, X.; Oruganti, A.; Yang, G.; Abe, H.; Wang, Y.; Tsubaki, N. Integrated tuneable synthesis of liquid fuels via Fischer–Tropsch technology. *Nat. Catal.* **2018,** 1, 787-793.

(4) Böller, B.; Durner, K. M.; Wintterlin, J. The active sites of a working Fischer–Tropsch catalyst revealed by operando scanning tunnelling microscopy. *Nat. Catal.* **2019,** 2, 1027-1034.

(5) Zhang, X.; Deng, J.; Lan, T.; Shen, Y.; Zhong, Q.; Ren, W.; Zhang, D. Promoting Methane Dry Reforming over Ni Catalysts via Modulating Surface Electronic Structures of BN Supports by Doping Carbon. *ACS Catal.* **2022**, 14152-14161.

(6) Zhang, X.; Deng, J.; Pupucevski, M.; Impeng, S.; Yang, B.; Chen, G.; Kuboon, S.; Zhong, Q.; Faungnawakij, K.; Zheng, L.; Wu, G.; Zhang, D. High-Performance Binary Mo–Ni Catalysts for Efficient Carbon Removal during

Carbon Dioxide Reforming of Methane. *ACS Catal.* **2021,** 11, 12087-12095.

(7) Song, Y.; Ozdemir, E.; Ramesh, S.; Adishev, A.; Subramanian, S.; Harale, A.; Albuali, M.; Fadhel, B. A.; Jamal, A.; Moon, D.; Choi, S. H.; Yavuz, C. T. Dry reforming of methane by stable Ni-Mo nanocatalysts on single-crystalline MgO. *Science* **2020,** 367, 777-781.

(8) Wang, Y.; Yao, L.; Wang, Y. N.; Wang, S. H.; Zhao, Q.; Mao, D. H.; Hu, C. W. Low-Temperature Catalytic CO_2 Dry Reforming of Methane on Ni-Si/ZrO_2 Catalyst. *ACS Catal.* **2018,** 8, 6495-6506.

(9) Liang, Z.; Li, T.; Kim, M.; Asthagiri, A.; Weaver, J. F. Low-temperature activation of methane on the IrO_2 (110) surface. *Science* **2017,** 356, 299-303.

(10) Deng, J.; Bu, K.; Shen, Y.; Zhang, X.; Zhang, J.; Faungnawakij, K.; Zhang, D. Cooperatively enhanced coking resistance via boron nitride coating over Ni-based catalysts for dry reforming of methane. *Appl. Catal. B: Environ.* **2022,** 302, 120859.

(11) Matsubu, J. C.; Zhang, S.; DeRita, L.; Marinkovic, N. S.; Chen, J. G.; Graham, G. W.; Pan, X.; Christopher, P. Adsorbate-mediated strong metal–support interactions in oxide-supported Rh catalysts. *Nat. Chem.* **2016,** 9, 120-127.

(12) Akri, M.; Zhao, S.; Li, X.; Zang, K.; Lee, A. F.; Isaacs, M. A.; Xi, W.; Gangarajula, Y.; Luo, J.; Ren, Y.; Cui, Y. T.; Li, L.; Su, Y.; Pan, X.; Wen, W.; Pan, Y.; Wilson, K.; Li, L.; Qiao, B.; Ishii, H.; Liao, Y. F.; Wang, A.; Wang, X.; Zhang, T. Atomically dispersed nickel as coke-resistant active sites for methane dry reforming. *Nat. Commun.* **2019,** 10, 5181.

(13) Tang, Y.; Wei, Y.; Wang, Z.; Zhang, S.; Li, Y.; Nguyen, L.; Li, Y.; Zhou, Y.; Shen, W.; Tao, F. F.; Hu, P. Synergy of Single-Atom Ni1 and Ru1 Sites on CeO_2 for Dry Reforming of CH4. *J. Am. Chem. Soc.* **2019,** 141, 7283-7293.

(14) Li, M. J.; Sun, Z. X.; Hu, Y. H. Catalysts for CO_2 reforming of CH4: a review. *J. Mater. Chem. A* **2021,** 9, 12495-12520.

(15) Lu, Y.; Guo, D.; Zhao, Y.; Moyo, P. S.; Zhao, Y.; Wang, S.; Ma, X. Enhanced catalytic performance of Nix-V@HSS catalysts for the DRM reaction: The study of interfacial effects on Ni-VOx structure with a unique yolk-shell structure. *J. Catal.* **2021,** 396, 65-80.

(16) Bhattar, S.; Abedin, M. A.; Kanitkar, S.; Spivey, J. J. A review on dry reforming of methane over perovskite derived catalysts. *Catal. Today* **2021,** 365, 2-23.

(17) Pakhare, D.; Spivey, J. A review of dry (CO_2) reforming of methane over noble metal catalysts. *Chem. Soc. Rev.* **2014,** 43, 7813-7837.

(18) Fang, S.; Hu, Y. H. Thermo-photo catalysis: a whole greater than the sum of its parts. *Chem Soc Rev* **2022,** 51, 3609-3647.

(19) Kim, C.; Hyeon, S.; Lee, J.; Kim, W. D.; Lee, D. C.; Kim, J.; Lee, H. Energy-efficient CO2 hydrogenation with fast response using photoexcitation of CO_2 adsorbed on metal catalysts. *Nat. Commun.* **2018,** 9, 3027.

(20) Tan, T. H.; Xie, B. Q.; Ng, Y. H.; Abdullah, S. F. B.; Tang, H. Y. M.; Bedford, N.; Taylor, R. A.; Aguey-Zinsou, K. F.; Amal, R.; Scott, J. Unlocking the potential of the formate pathway in the photo-assisted Sabatier reaction. *Nat. Catal.* **2020,** 3, 1034-1043.

(21) Mai, H. X.; Sun, L. D.; Zhang, Y. W.; Si, R.; Feng, W.; Zhang, H. P.; Liu, H. C.; Yan, C. H. Shape-selective synthesis and oxygen storage behavior of ceria nanopolyhedra, nanorods, and nanocubes. *J. Phys. Chem. B* **2005,** 109, 24380-24385.

(22) Yang, W. T.; Wang, X.; Song, S. Y.; Zhang, H. J. Syntheses and Applications of Noble-Metal-free CeO_2-Based Mixed-Oxide Nanocatalysts. *Chem* **2019,** 5, 1743-1774.

(23) Muravev, V.; Spezzati, G.; Su, Y. Q.; Parastaev, A.; Chiang, F. K.; Longo, A.; Escudero, C.; Kosinov, N.; Hensen, E. J. M. Interface dynamics of Pd-CeO_2 single-atom catalysts during CO oxidation. *Nat. Catal.* **2021,** 4, 469-478.

(24) Xing, F.; Nakaya, Y.; Yasumura, S.; Shimizu, K.-i.; Furukawa, S. Ternary platinum-cobalt-indium nanoalloy on ceria as a highly efficient catalyst for the oxidative dehydrogenation of propane using CO_2. *Nat. Catal.* **2022,** 5, 55-65.

(25) Prats, H.; Gutiérrez, R. A.; Piñero, J. J.; Viñes, F.; Bromley, S. T.; Ramírez, P. J.; Rodriguez, J. A.; Illas, F. Room Temperature Methane Capture and Activation by Ni Clusters Supported on TiC(001): Effects of Metal–Carbide Interactions on the Cleavage of the C–H Bond. *J. Am. Chem. Soc.* **2019,** 141, 5303-5313.

(26) Zhang, F.; Liu, Z.; Chen, X.; Rui, N.; Betancourt, L. E.; Lin, L.; Xu, W.; Sun, C.-j.; Abeykoon, A. M. M.; Rodriguez, J. A.; Teržan, J.; Lorber, K.; Djinović, P.; Senanayake, S. D. Effects of Zr Doping into Ceria for the Dry Reforming of Methane over Ni/CeZrO2 Catalysts: In Situ Studies with XRD, XAFS, and AP-XPS. *ACS Catal.* **2020**, 3274-3284.

(27) Chen, A.; Yu, X.; Zhou, Y.; Miao, S.; Li, Y.; Kuld, S.; Sehested, J.; Liu, J.; Aoki, T.; Hong, S.; Camellone, M. F.; Fabris, S.; Ning, J.; Jin, C.; Yang, C.; Nefedov, A.; Wöll, C.; Wang, Y.; Shen, W. Structure of the catalytically active copper-ceria interfacial perimeter. *Nat. Catal.* **2019,** 2, 334-341.

(28) Jones, J.; Xiong, H.; DeLaRiva, A. T.; Peterson, E. J.; Pham, H.; Challa, S. R.; Qi, G.; Oh, S.; Wiebenga, M. H.; Pereira Hernandez, X. I.; Wang, Y.; Datye, A. K. Thermally stable single-atom platinum-on-ceria catalysts via atom trapping. *Science* **2016,** 353, 150-154.

(29) Funke, H.; Scheinost, A. C.; Chukalina, M. Wavelet analysis of extended x-ray absorption fine structure data. *Phys. Rev. B* **2005,** 71, 094110.

(30) Zhang, H.; Yu, L.; Chen, T.; Zhou, W.; Lou, X. W. D. Surface Modulation of Hierarchical MoS_2 Nanosheets by Ni Single Atoms for Enhanced Electrocatalytic Hydrogen Evolution. *Adv. Funct. Mater.* **2018,** 28, 1807086.

(31) Campuzano, J. C.; Greenler, R. G. The adsorption sites of CO on Ni(111) as determined by infrared reflection-absorption spectroscopy. *Surf. Sci.* **1979,** 83, 301-312.

(32) Layman, K. A.; Bussell, M. E. Infrared Spectroscopic Investigation of CO Adsorption on Silica-Supported Nickel Phosphide Catalysts. *J. Phys. Chem. B* **2004,** 108, 10930-10941.

(33) Xu, M.; Yao, S.; Rao, D.; Niu, Y.; Liu, N.; Peng, M.; Zhai, P.; Man, Y.; Zheng, L.; Wang, B.; Zhang, B.; Ma, D.; Wei, M. Insights into Interfacial Synergistic Catalysis over Ni@TiO_{2-x} Catalyst toward Water-Gas

Shift Reaction. *J. Am. Chem. Soc.* **2018,** 140, 11241-11251.

(34) Heine, C.; Lechner, B. A.; Bluhm, H.; Salmeron, M. Recycling of CO_2: Probing the Chemical State of the Ni(111) Surface during the Methanation Reaction with Ambient-Pressure X-Ray Photoelectron Spectroscopy. *J Am Chem Soc* **2016,** 138, 13246-13252.

(35) Zhou, L. A.; Martirez, J. M. P.; Finzel, J.; Zhang, C.; Swearer, D. F.; Tian, S.; Robatjazi, H.; Lou, M. H.; Dong, L. L.; Henderson, L.; Christopher, P.; Carter, E. A.; Nordlander, P.; Halas, N. J. Light-driven methane dry reforming with single atomic site antenna-reactor plasmonic photocatalysts. *Nat. Energy* **2020,** 5, 61-70.

(36) Rao, Z.; Cao, Y.; Huang, Z.; Yin, Z.; Wan, W.; Ma, M.; Wu, Y.; Wang, J.; Yang, G.; Cui, Y.; Gong, Z.; Zhou, Y. Insights into the Nonthermal Effects of Light in Dry Reforming of Methane to Enhance the H_2/CO Ratio Near Unity over Ni/Ga_2O_3. *ACS Catal.* **2021**, 4730-4738.

(37) Wang, C.; Jie, X.; Qiu, Y.; Zhao, Y.; Al-Megren, H. A.; Alshihri, S.; Edwards, P. P.; Xiao, T. The importance of inner cavity space within Ni@SiO_2 nanocapsule catalysts for excellent coking resistance in the high-space-velocity dry reforming of methane. *Appl. Catal. B* **2019,** 259, 118019.

(38) Liu, Z. Y.; Grinter, D. C.; Lustemberg, P. G.; Nguyen-Phan, T. D.; Zhou, Y. H.; Luo, S.; Waluyo, I.; Crumlin, E. J.; Stacchiola, D. J.; Zhou, J.; Carrasco, J.; Busnengo, H. F.; Ganduglia-Pirovano, M. V.; Senanayake, S. D.; Rodriguez, J. A. Dry Reforming of Methane on a Highly-Active Ni-CeO_2 Catalyst: Effects of Metal-Support Interactions on C-H Bond Breaking. *Angew. Chem. Int. Ed. Engl.* **2016,** 55, 7455-7459.

(39) El-Roz, M.; Bazin, P.; Daturi, M.; Thibault-Starzyk, F. Operando Infrared (IR) Coupled to Steady-State Isotopic Transient Kinetic Analysis (SSITKA) for Photocatalysis: Reactivity and Mechanistic Studies. *ACS Catal.* **2013,** 3, 2790-2798.

(40) Wang, F.; He, S.; Chen, H.; Wang, B.; Zheng, L.; Wei, M.; Evans, D. G.; Duan, X. Active Site Dependent Reaction Mechanism over Ru/CeO_2 Catalyst toward CO2 Methanation. *J. Am. Chem. Soc.* **2016,** 138, 6298-305.

(41) Wu, C.; Lin, L.; Liu, J.; Zhang, J.; Zhang, F.; Zhou, T.; Rui, N.; Yao, S.; Deng, Y.; Yang, F.; Xu, W.; Luo, J.; Zhao, Y.; Yan, B.; Wen, X. D.; Rodriguez, J. A.; Ma, D. Inverse ZrO_2/Cu as a highly efficient methanol synthesis catalyst from CO_2 hydrogenation. *Nat. Commun.* **2020,** 11, 5767.

(42) Rezvani, A.; Abdel-Mageed, A. M.; Ishida, T.; Murayama, T.; Parlinska-Wojtan, M.; Behm, R. J. CO_2 Reduction to Methanol on Au/CeO_2 Catalysts: Mechanistic Insights from Activation/Deactivation and SSITKA Measurements. *ACS Catal.* **2020,** 10, 3580-3594.

(43) Xie, B.; Kumar, P.; Tan, T. H.; Esmailpour, A. A.; Aguey-Zinsou, K.-F.; Scott, J.; Amal, R. Doping-Mediated Metal–Support Interaction Promotion toward Light-Assisted Methanol Production over Cu/ZnO/Al_2O_3. *ACS Catal.* **2021**, 5818-5828.

(44) Parastaev, A.; Muravev, V.; Osta, E. H.; van Hoof, A. J. F.; Kimpel, T. F.; Kosinov, N.; Hensen, E. J. M. Boosting CO_2 hydrogenation via size-dependent metal-support interactions in cobalt/ceria-based catalysts. *Nat. Catal.* **2020,** 3, 526-533.

(45) Zhou, J.; Gao, Z.; Xiang, G.; Zhai, T.; Liu, Z.; Zhao, W.; Liang, X.; Wang, L. Interfacial compatibility critically controls Ru/TiO_2 metal-support interaction modes in CO_2 hydrogenation. *Nat Commun* **2022,** 13, 327.

(46) Hu, J.; Yu, L.; Deng, J.; Wang, Y.; Cheng, K.; Ma, C.; Zhang, Q.; Wen, W.; Yu, S.; Pan, Y.; Yang, J.; Ma, H.; Qi, F.; Wang, Y.; Zheng, Y.; Chen, M.; Huang, R.; Zhang, S.; Zhao, Z.; Mao, J.; Meng, X.; Ji, Q.; Hou, G.; Han, X.; Bao, X.; Wang, Y.; Deng, D. Sulfur vacancy-rich MoS_2 as a catalyst for the hydrogenation of CO_2 to methanol. *Nat. Catal.* **2021,** 4, 242-250.

(47) Galhardo, T. S.; Braga, A. H.; Arpini, B. H.; Szanyi, J.; Goncalves, R. V.; Zornio, B. F.; Miranda, C. R.; Rossi, L. M. Optimizing Active Sites for High CO Selectivity during CO_2 Hydrogenation over Supported Nickel Catalysts. *J. Am. Chem. Soc.* **2021,** 143, 4268-4280.

(48) Shoji, S.; Bin Mohd Najib, A. S.; Yu, M.-W.; Yamamoto, T.; Yasuhara, S.; Yamaguchi, A.; Peng, X.; Matsumura, S.; Ishii, S.; Cho, Y.; Fujita, T.; Ueda, S.; Chen, K.-P.; Abe, H.; Miyauchi, M. Charge partitioning by intertwined metal-oxide nano-architectural networks for the photocatalytic dry reforming of methane. *Chem Catal.* **2022,** 2, 321-329.

(49) Zhao, Y. X.; Yang, B.; Li, H. F.; Zhang, Y.; Yang, Y.; Liu, Q. Y.; Xu, H. G.; Zheng, W. J.; He, S. G. Photoassisted Selective Steam and Dry Reforming of Methane to Syngas Catalyzed by Rhodium–Vanadium Bimetallic Oxide Cluster Anions at Room Temperature. *Angew. Chem. Int. Ed. Engl.* **2020,** 59, 21216-21223.

Table of Contents